Article

Effect of Strain Rate and Temperature on Tensile and Fracture Performance of AA2050-T84 Alloy

Nagaraj Ekabote [1], Krishnaraja G. Kodancha [1,*], T. M. Yunus Khan [2,3] and Irfan Anjum Badruddin [3]

1   School of Mechanical Engineering, KLE Technological University, Hubballi 580031, India;
     ekabotenagaraj@gmail.com
2   Research Center for Advanced Materials Science (RCAMS), King Khalid University, 9004,
     Abha 61413, Saudi Arabia; yunus.tatagar@gmail.com
3   Department of Mechanical Engineering, College of Engineering, King Khalid University, 394,
     Abha 61421, Saudi Arabia; magami.irfan@gmail.com
*   Correspondence: krishnaraja@kletech.ac.in; Tel.: +91-98-8659-6953

Abstract: AA2050-T84 alloy is widely used in primary structures of modern transport aircraft. AA2050-T84 is established as a low-density aluminum alloy with improved Young's modulus, less anisotropy, and temperature-dependent mechanical properties. During flights, loading rate and temperature variation in aircraft engine subsequent parts are commonly observed. The present work focuses on the effect of loading rate and temperature on tensile and fracture properties of the 50 mm thick (2-inch) AA2050-T84 alloy plate. Quasi-static strain rates of 0.01, 0.1, and 1 s^{-1} at $-20\ °C$, 24 °C and 200 °C are considered. Tensile test results revealed the sensitivity of mechanical properties towards strain rate variations for considered temperatures. The key tensile properties, yield, and ultimate tensile stresses were positive strain rate dependent. However, Young's modulus and elongation showed negative strain rate dependency. Experimental fracture toughness tests exhibited the lower Plane Strain Fracture Toughness (K_{IC}) at $-20\ °C$ compared to 24 °C. Elastic numerical fracture analysis revealed that the crack driving and constraint parameters are positive strain rate dependent and maximum at $-20\ °C$, if plotted and analyzed over the stress ratio. The current results concerning strain rates and temperatures will help in understanding the performance-related issues of AA2050-T84 alloy reported in aircraft applications.

Keywords: AA2050-T84 alloy; strain rate effect; plane strain fracture toughness; temperature effect; strain rate effect; constraint effect

1. Introduction

Modern aircraft predominantly use lightweight structures to improve the performance-to-weight ratio. The low-density Aluminum alloy is popular among aircraft structures owing to its durable mechanical properties and ease of manufacturability [1,2]. Composites pose tough competition to Aluminum alloys due to their tailor-made properties suited for specific applications. The unpredictable behavior of composites for change in temperature and time, restricted its usage to secondary and tertiary aircraft structures [3]. Currently, the modern transport aircraft primary structures are built by Al-Li alloys. The Lithium addition to aluminum with improved manufacturing methods resulted in the enhancement of specific strength and stiffness of the alloy [4]. However, the higher cost of Al-Li alloy restricted its usage to only aerospace industries.

The apprehensions related to diversifying mechanical properties of 1st and 2nd generation Al-Li alloys directed the complete withdrawal from aerospace applications [2]. Some noteworthy limitations were anisotropic behavior, cracking during manufacturing, and thermal instability-driven lower fracture toughness [2]. The skillful and sophisticated fabrication methods steered the evolution of 3rd generation Al-Li alloys. The spars and ribs of modern transport aircraft are fabricated by a 3rd generation Al-Li alloy, AA2050-T84 [1].

AA2050-T84 alloy exhibits exceptional tensile, fatigue, and fracture toughness behavior suited for damage tolerance property requirements of wing structures [1]. Notably, the anisotropic behavior and temperature-dependent property variations of AA2050-T84 alloy were also reported [5,6]. During flights, the fuel pressure at various altitudes of an aircraft, wing lift, and drag loads at different operating conditions may result in load rate and temperature variations on spars and ribs. The sensitivity of AA2050-T84 alloy to these load and temperature variations are essential to claim its suitability to modern transport aircraft wing parts. The following paragraphs discuss the strain rate and temperature effect on various ductile and brittle material properties reported in the literature.

Mirza et al. [7] have conducted tensile tests on mild steel and aluminum at various quasi-static (lower strain rates up to $1 \, \mathrm{s}^{-1}$) strain rates. The results have shown negligible dependency of ductility on strain rate variations. Clausen et al. [8] have reported the negative strain rate sensitivity of AA5083–H116 through tensile tests for quasi-static strain rate variations. The strain rate dependency was related to dynamic strain aging at lower strain rates and temperatures, resulting in serrated stress-strain curves. Singh et al. [9] have reported increased flow stress with the rise in test temperature and strain rates on titanium alloys. The observed trend was attributed to the dynamic strain aging of the alloy. Through experiments and numerical analysis, Khan et al. [10] have investigated the influence of strain rate and temperature on Al2024-T351. The results inferred a strong temperature dependency and negligible strain rate effect on fracture strength of the Al2024-T351 alloy. Anderson et al. [11] have witnessed the sensitivity of DP 780 steel towards the strain rate variations. The tensile stress-strain response was steady and almost negligible concerning quasi-static strain rates. The alterations in failure surface morphology were noticed with changes in strain rates.

The experimental tensile results on DP590 and TRIP 780 steel by Roth et al. [12] have shown that ductility increases with loading speed. Rincon et al. [13] have studied the influence of temperature (between $-90 \, ^\circ\mathrm{C}$ to $270 \, ^\circ\mathrm{C}$) on tensile behavior of an as-cast A319 alloy and noticed the silicon dominant brittle fracturing regardless of temperature variation. Natesan et al. [14] have reported the variation in strain rate effect at different temperatures on the deformation behavior of A356-T7 cast aluminum alloys. The yield stress and strain hardening of Aluminum alloy 7075-W exhibited the positive load rate effect and negative temperature effect through plasticity experiments [15]. Hafley et al. [5] and Chemin et al. [6] have reported AA2050-T84 alloy tensile and fracture properties sensitivity to temperature variations. In summary, the material properties of various alloys of steel and aluminum generally exhibit reliance on strain rate and temperature and are noteworthy.

The dependency of fracture behavior on strain rate and temperature mainly alters the state of stress near the crack front. The state of stress variation at the crack front due to specimen type, geometry, and load type was defined by a term constraint. The constraint level at the crack component/structure drives the selection of standard test specimens for fracture toughness tests [16,17]. In Linear Elastic Fracture Mechanics (LEFM), the variation of the state of stress near the crack was measured by popular constraint parameters [18–26]. T_{11} and T_{33} are used to measure the in-plane and out-of-plane constraints in LEFM. The variations of T_{11} and T_{33} concerning specimen type, geometry, and load were well documented [16,18–26]. However, the strain rate effect at different temperatures on tensile and fracture behavior of the AA2050-T84 alloy is essential to claim its suitability to primary structures of the aircraft wing. Fracture toughness standard methods recommend the single value of fracture toughness for quasi-static load variations [27]. Notably, the above literature study shows the strong dependency of material properties on strain rate and temperature variations. Moreover, critical cracks were observed in AA2050-T84 made spars and ribs of Airbus-380 aircraft after a few flights [28]. The present literature findings demand a fracture study based on constraints near the crack of AA2050-T84 alloy at different strain rates and temperatures.

In the present work, AA2050-T84 alloy tensile behavior at different strain rates and temperatures are experimentally studied. Experimental fracture toughness tests are con-

ducted using Compact Tension (C(T)) specimens at various temperatures. Furthermore, the effect of strain rate on fracture characterizing parameters in LEFM such as Stress Intensity Factor (K_I), T_{11}, and T_{33} are analyzed numerically for different temperatures. Finally, the AA2050-T84 alloy tensile and fracture behavior dependency on strain rates and temperatures are compared and evaluated for compatibility for aircraft wing structures.

2. Material and Test Details

2.1. AA2050-T84 Alloy

This study uses a 50 mm thick (2-inch) AA2050-T84 alloy plate to extract the test specimens. The chemical composition of AA2050-T84 alloy in wt% as obtained from the supplier is shown in Table 1. Copper is used in AA2050-T84 to provide high strength, suited for aircraft applications [29]. The Lithium addition is (<1%) restricted to balance between density reduction and increase in Young's modulus of the alloy [3,29].

Table 1. Chemical composition of 50 mm thick (2-inch) AA2050-T84 alloy plate (wt%).

Cu	Mg	Mn	Zn	Fe	Ti	Si	Li	Zr	Ag	Al
3.743	0.369	0.372	0.025	0.045	0.040	0.039	0.798	0.087	0.398	Base

2.2. Tensile and Fracture Toughness Test

ASTM E8/E8M-21, the standard test method for tension testing of metallic materials [30], was used for the tensile specimen preparation and testing of AA2050-T84 alloy. Round specimens were extracted in the rolling (along the length of the plate) direction of the AA2050-T84 plate. Figure 1 shows the tensile test specimen dimensions (in mm) used in this study. The main dimensions of the specimen are, gauge diameter (D_0 = 6 mm), gauge length (L_0 = 30 mm), and overall specimen length (L = 65 mm). The tensile specimens were designed, keeping the L_0/D_0 ratio to 5.
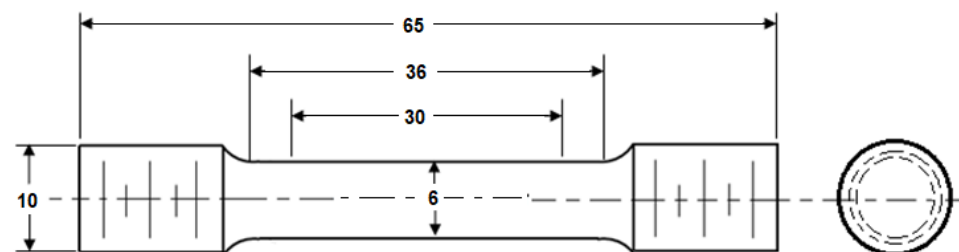

Figure 1. Tensile test specimen. All dimensions are in mm.

ASTM E399-20a, the standard test method for linear-elastic plane strain fracture toughness of metallic materials [27], was used. The commonly used fracture test specimen for primary aircraft structures is the compact tension (C(T)) specimen shown in Figure 2. The standard dimensions (in mm) are specimen width (W = 25.4 mm), specimen height (H = 2W), and specimen thickness (B) = crack length (a) = 0.5W. The C(T) specimen is extracted, ensuring the crack length in the rolling direction and load application in the transverse directions of the plate.

Flight durations and operations cause the temperature variations of the wing parts. Furthermore, the effect of these variations depends on alloy type and its ductile to brittle transition temperature [31]. However, temperature variations will be high near the aircraft engine (wing components), and the experienced load rates are dynamic. In the present study, the quasi-static strain rates considered in the tensile tests were 0.01, 0.1, and 1 s^{-1}. The temperatures considered were −20 °C (Sub-zero temperature), 24 °C (Room temperature), and 200 °C (High temperature) [32]. In the tensile and fracture toughness tests, the low-temperature chamber with liquid nitrogen and a high-temperature furnace with forced convection heating was used to maintain the sub-zero and high temperatures.

The Servo Electric Universal Testing Machine (UTM) (BISS, Bangalore, India) with 50 kN capacity was used for tensile and fracture toughness tests. In tensile testing, the applied load and deformations were recorded continuously through the load cell and extensometer, respectively. However, along with these, Crack Opening Displacement (COD) gauge (BISS, Bangalore, India) was used to record the relative displacement of two knife edges of the C(T) specimen in the fracture toughness test. These data were further processed to extract the tensile properties and fracture toughness of the AA2050-T84 alloy as per standards [27,30].
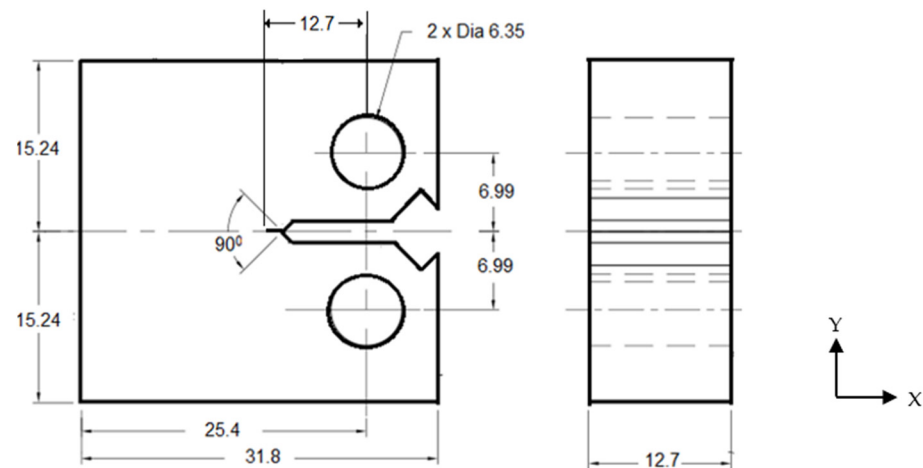

Figure 2. Compact Tension (C(T)) Specimen. All dimensions are in mm.

2.3. Finite Element Analysis

The crack driving forces and constraints of the C(T) specimen were investigated at different load rates and temperatures using 3D linear elastic finite element analysis (FEA). Half-symmetry is modeled and analyzed using Abaqus (6.14, 2014, Dassault Systemes Simulia Corp., Providence, RI, USA). The Poisson's ratio (v) and Young's modulus (E) obtained from experimentally conducted tensile results at different strain rates and temperatures are used for linear elastic fracture analysis. The output parameters viz. stress intensity factor (K_I) and constraint parameter (T_{11}) were extracted using the counter-integral method mentioned in Abaqus post-processor [33]. T_{33} is calculated by using Equation (1). In Equation (1), ε_{33} is a strain in the *z*-direction (thickness direction) extracted along the crack front. The material property input and the K_I extraction details were adopted as similar to the work of [22,33].

$$T_{33} = E\varepsilon_{33} + vT_{11} \tag{1}$$

Half symmetry C(T) meshed model with supports and loading is shown in Figure 3. 20-noded hexahedral elements with reduced integration were used for the meshing. A fine mesh near the crack front was used to encapsulate the crack characteristics effectively. Singularity at the crack front was emulated by shifting the mid-side nodes of crack surrounding elements towards the crack front. The crack edge (crack front) surrounded by these nodes is defined as contour integral. The output parameters are calculated along the user-defined contour integrals (in the present analysis, it is 10 contours). The detailed procedure to define the crack front and contour integrals to obtain crack driving parameters is available in the Abaqus manual [33]. Y-symmetry was imposed along the ligament (the uncracked portion in the crack plane), and the tensile load was applied through the hole to simulate Mode-I.
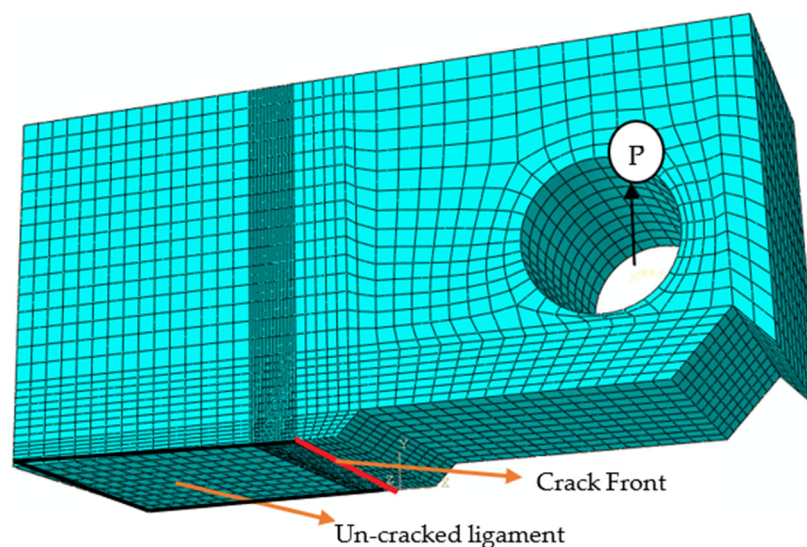
Figure 3. C(T) Meshed Model with Boundary conditions.

3. Results and Discussions

The following sections discuss the experimental and numerical analysis of the AA2050-T84 alloy.

3.1. Experimental Analysis

3.1.1. Tensile Test Analysis

The experimental tensile tests were conducted at varying temperatures and strain rates. A total of 27 tensile tests were conducted, comprising 3 experiments for each strain rate per temperature. The stress-strain curves for different strain rates and temperatures are shown in Figure 4a. The corresponding variation of average tensile properties viz. yield stress (σ_{ys}), ultimate tensile stress (σ_{ut}), Young's modulus (E), and % elongation (% et) extracted from the stress-strain curves along with error bars are presented in Figure 4b–e. The positive strain rate dependency was observed for tensile yield stress for the temperatures considered in the study, as shown in Figure 4b. The highest yield stress variation of 2% between 0.01 s^{-1} to 0.1 s^{-1} and 0.1 s^{-1} to 1 s^{-1} was observed at -20 °C. However, the lowest yield stress variation between successive strain rates, around 0.5%, was noticed at 24 °C. It was observed that the yield stress decreased from -20 °C to room temperature and further increased slightly at 200 °C, indicating the V-shaped behavior for temperature variation.

Similarly, ultimate tensile stress exhibited the positive strain rate dependency at various temperatures, as shown in Figure 4c. However, strain rate has minimal effect on ultimate tensile stress as the difference observed between successive strain rates for all temperatures is less than 1%. The ultimate tensile stress is inversely proportional to the temperature for all the strain rates and is in line with the observations of Hafley et al. [5] and Chemin et al. [6]

Figure 4d, shows the variation of Young's modulus at various strain rates and temperatures. Young's modulus showed negative strain rate sensitivity at room and higher temperatures. However, the strain rate effect on Young's modulus was negligible (around 1%) at -20 °C. The maximum Young's modulus difference of about 10% was observed at 200 °C between strain rates 0.01 and 1 s^{-1}. Furthermore, Young's modulus difference was around 5% at room temperature for successive strain rate variations. This reveals that the strain rate sensitivity towards Young's modulus was in the decreasing order of temperatures 200 °C:24 °C:-20 °C. At 200 °C. Young's modulus values were minimal and almost similar in values at -20 °C.
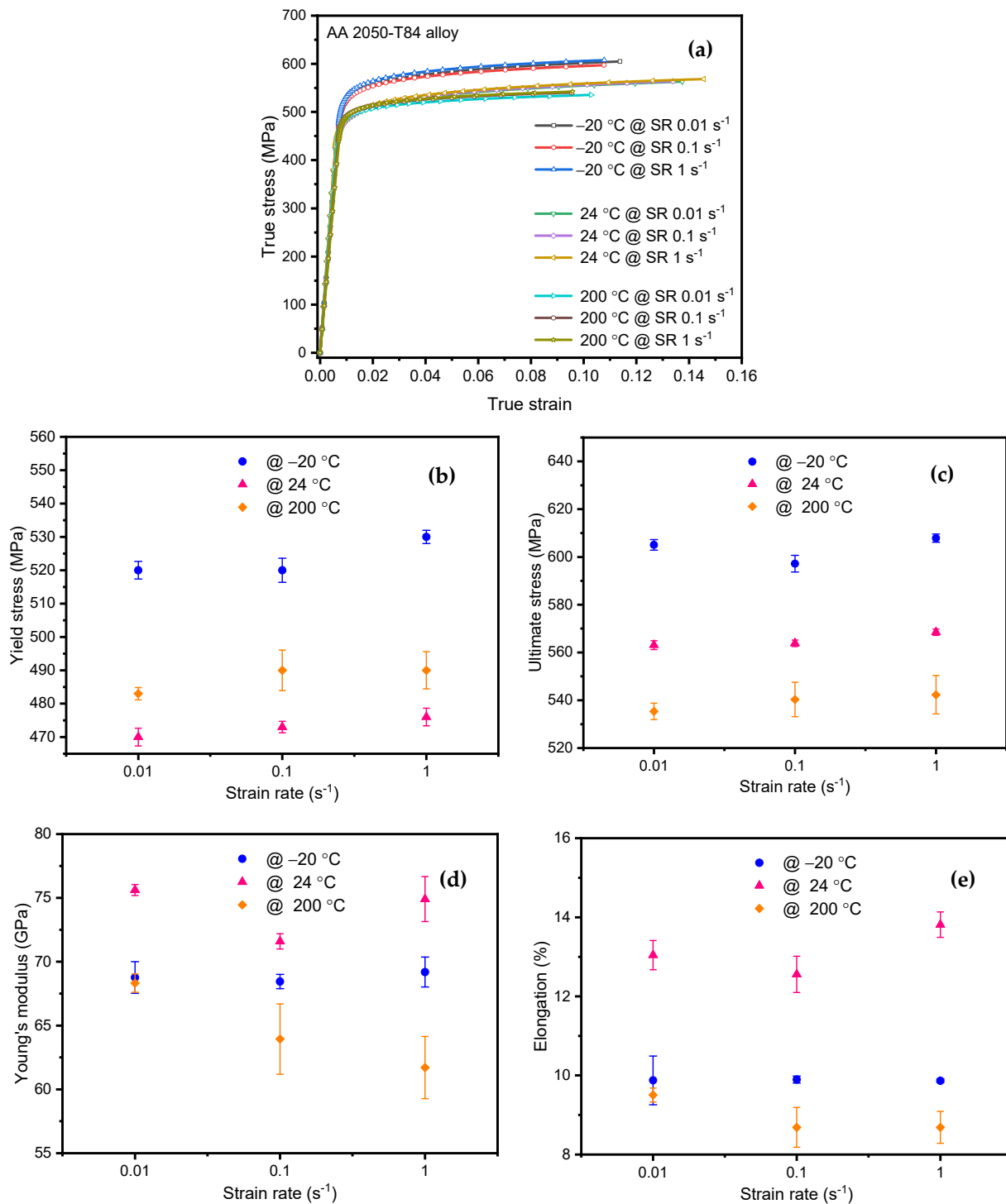
Figure 4. Strain rate and Temperature effect on: (**a**) True stress-strain curves (**b**) Yield stress; (**c**) Ultimate stress; (**d**) Young's modulus; (**e**) elongation.

Overall, a reduction between 6% and 10% is noticed in Young's modulus for the temperatures studied. The exact thickness of the plate with room temperature and −54 °C has been studied by Chemin et al. [6], revealing the same trend with a 2.5% reduction in Young's modulus. With a 100 mm (4-inch) plate, Hafley et al. [5] noticed a 9–11% reduction in Young's modulus when studied at different locations for room and −196 °C temperature.

Strong interatomic bonding between the atoms at room temperature may be the probable reason for the highest value of Young's modulus. Farraro and McLellan [34]

have reported that the lower values of Young's modulus at elevated temperature indicate weakened interatomic bonding between the atoms.

Figure 4e shows the % elongation of AA2050-T84 alloy at different strain rates and temperatures. Negative strain rate dependency on % elongation as similar to Young's modulus was observed for various temperatures. The maximum % elongation was noticed at room temperature, indicating higher ductility than other temperatures.

3.1.2. Fracture Toughness Test Analysis

The fracture toughness tests were conducted as per ASTM E399-20a at different temperatures. ASTM E399-20a essentially elucidates the procedure of obtaining the single value, Plane Strain Fracture Toughness (K_{IC}), for metallic materials under quasi-static strain rates. The C(T) specimen was fatigue pre-cracked to emulate the natural crack characteristics. The effect of loading and material properties (mainly yield stress) strongly influences fatigue crack growth [35]. The pre-cracking load details are shown in Table 2. The load ratio ($\sigma_{min}/\sigma_{max}$) was maintained at 0.1 to attain the a/W range in between 0.45 and 0.55.

Table 2. Pre-cracking details of fracture toughness test.

Crack Length a (mm)	Crack Length/Width a/W	Maximum Stress σ_{max} (MPa)	Minimum Stress σ_{min} (MPa)	Mean Stress σ_{mean} (MPa)	Alternating Stress $\sigma_{average}$ (MPa)
12.94	0.51	250	25	137.5	112.5

The pre-cracked C(T) specimen was tested under Mode-I (opening mode) loading through tensile load application at the holes. A minimum of 3 successful fracture toughness tests was conducted at each temperature at the strain rate 0.01 s^{-1}. The K_{IC} (average of 3 test samples) obtained from experiments for −20 °C and 24 °C are 904.28 and 1059.36 MPa mm$^{1/2}$, respectively. The error bar for the K_{IC} is depicted in Figure 5.

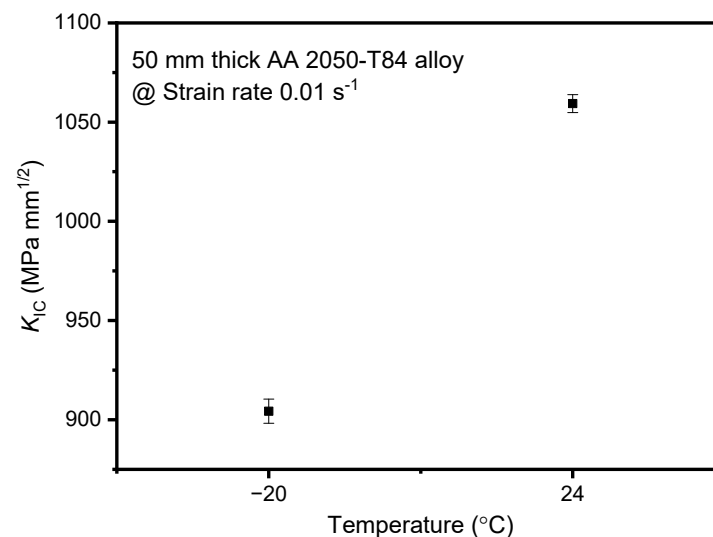**Figure 5.** Plane Strain Fracture Toughness (K_{IC}) at various temperatures.

At 200 °C, all the 3 test results were invalid as the ample crack deviation was observed from the crack plane. However, the K_{IC} has reduced by about 15% from room to sub-zero temperature. Similarly, in the work of Chemin et al. [6], a reduction of the order of magnitude 16% in K_{IC} was noticed in the rolling direction of the AA2050-T84 alloy plate from room to cryogenic (−56 °C) temperature. The decrease of K_{IC} at sub-zero temperatures of AA2050-T84 alloy can be attributed to surface hardening inside the grain and validated by the grain microstructure of the alloy [6,36]. In summary, the positive

temperature dependency was witnessed for K_{IC} of AA2050-T84 alloy at strain rate 0.01 s^{-1}. The economic limitations on conducting further fracture toughness tests at other strain rates impelled us to adopt the numerical analysis.

3.2. Linear Elastic Fracture Analysis

ASTM E399-20a, to predict the K_{IC} of metallic materials, recommended the single toughness value for lower strain rate variations. However, the variation of tensile properties of AA2050-T84 alloy at different lower strain rates and temperatures was substantial. The elastic fracture analysis was carried out at varied strain rates and temperatures using the Abaqus software. The current numerical procedure was adopted from Kudari et al. [22] and Kavale et al. [37] The K_I values extracted through-thickness direction of the crack at 24 °C conditions, and experimental K_{IC} are shown in Figure 6. The experimental K_{IC} value was emulated through numerical fracture analysis with less than 1% error, as observed in Figure 6.
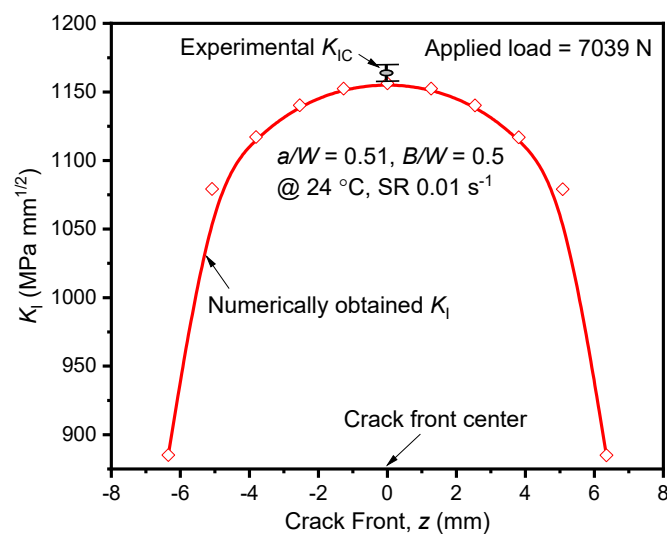

Figure 6. Stress intensity factor (K_I) along the crack front at 24 °C.

Similarly, at −20 °C, the validation of the numerical procedure was executed with less than 1% error. For all the numerical analysis, the center of the crack front was associated with the largest value of the crack characterizing parameter. Thus, the K_I values at the center of the specimen are used for analysis in further discussions.

3.2.1. Effect of Strain Rate

In linear elastic fracture analysis, the experimental load associated with K_{IC} of the alloy is the applied load at respective temperatures. However, the K_{IC} at 200 °C was unavailable, and hence for the numerical analysis, the assumed load applied up to K_I = 1200 MPa mm$^{1/2}$. The applied stress ($\sigma_{applied}$) was determined using the relationship mentioned in Equation (2) [27]. The extracted values of K_I at the crack front center for various strain rates and temperatures are plotted against the stress ratio ($\sigma_{applied}/\sigma_{ys}$) as shown in Figure 7. Positive strain rate dependency of the K_I was observed for all temperatures considered in this study. At room temperature, a steady increase of 0.6% in K_I was witnessed with the rise in strain rate. However, for strain rate 1 s^{-1}, the maximum of 1.88% increase in K_I was noticed at −20 °C. The strain rate sensitivity on K_I was found to be maximum at −20 °C and minimum at 24 °C, as the same trend was noticed for tensile yield stress values. The results of the K_I are in line with the yield stress variations of the alloy for all strain rates at different temperatures. The nominal variations of K_I (within the stress ratio of K_{IC}) indicate the negligible dependency of fracture characterizing parameters on strain rates for AA2050-T84 alloy. Moreover, ASTM

E399-20a recommendation to use the single value of K_{IC} for quasi-static strain rates seems to be justifying as the difference in numerical K_I values was minimal.

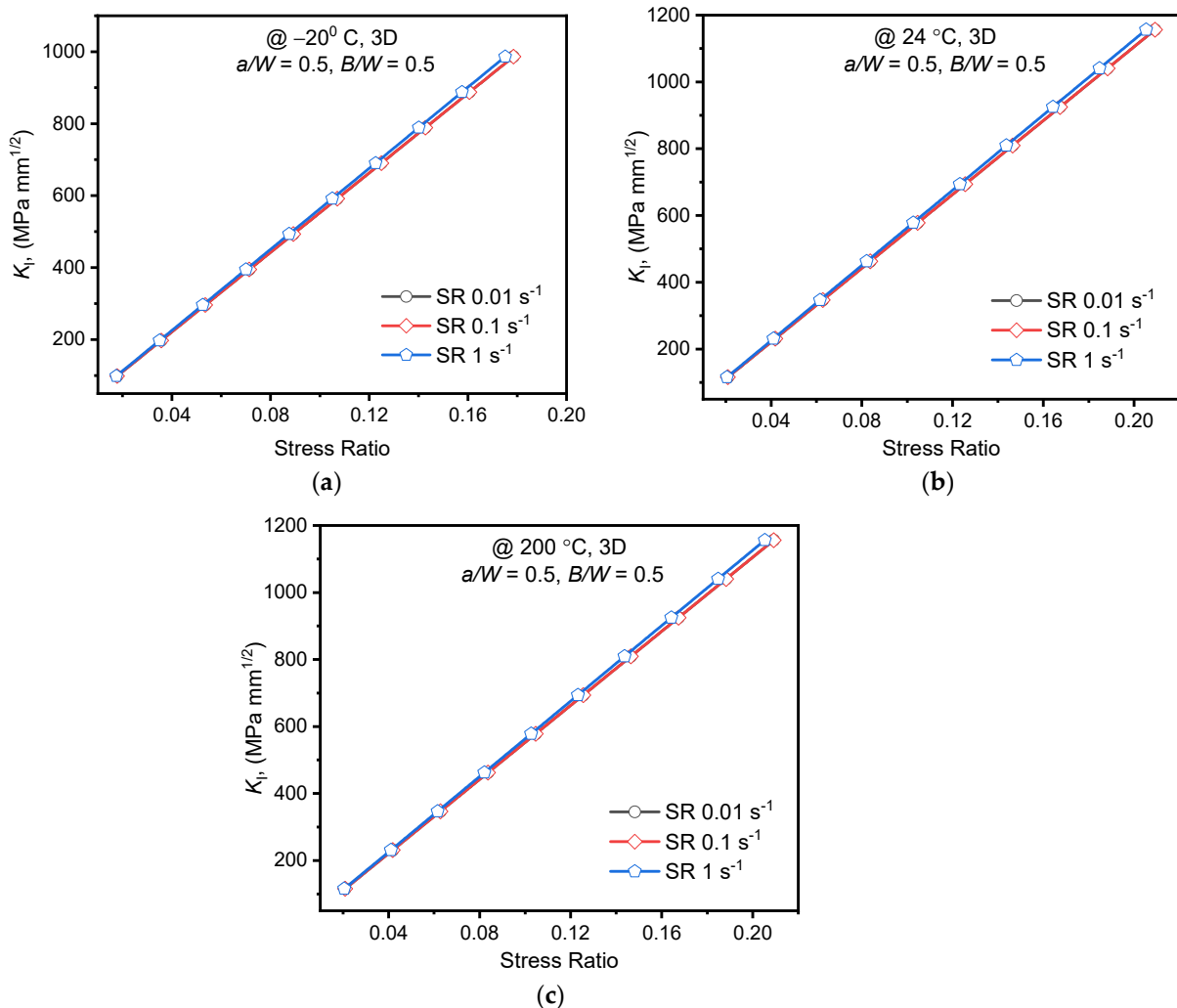$$K_I = \frac{P_{\text{applied}}}{B\sqrt{W}}\, f\left(\frac{a}{W}\right) \tag{2}$$

Figure 7. K_I at specimen thickness center obtained using FEA for different strain rates vs. Stress ratio (**a**) @ −20 °C; (**b**) 24 °C; (**c**) 200 °C.

Further, the effect of strain rate on crack tip/front constraints has been evaluated through T_{11} and T_{33}. The values of T_{11} and T_{33} are found to vary along the thickness similar to K_I variation and maximum being at the center of the specimen. One can infer that the crack-front constraint is high at the center than at the surface; the material may fail at the center than on surface or shows instability at the center of the specimen. As the constraint parameters do not have a unique value for the specimen thickness, maximum values at the center of the specimen are considered for further analysis. T_{11} and T_{33} variations for different strain rates within the purview of K_{IC} (or stress ratio) of the alloy at respective temperatures are plotted in Figure 8. The nature of variation was identical at all strain rates for both constraint parameters. However, the increase in stress ratio resulted in positive T_{11} and negative T_{33} values at all strain rates and temperatures. It is clear from Figure 8, that the applied stress was directly proportional to T_{11} and inversely proportional to T_{33}. The negative strain along the thickness resulted in the negative T_{33} [20]. This is in close agreement with the findings of Kudari et al. [22] for IF steel C(T) specimen.
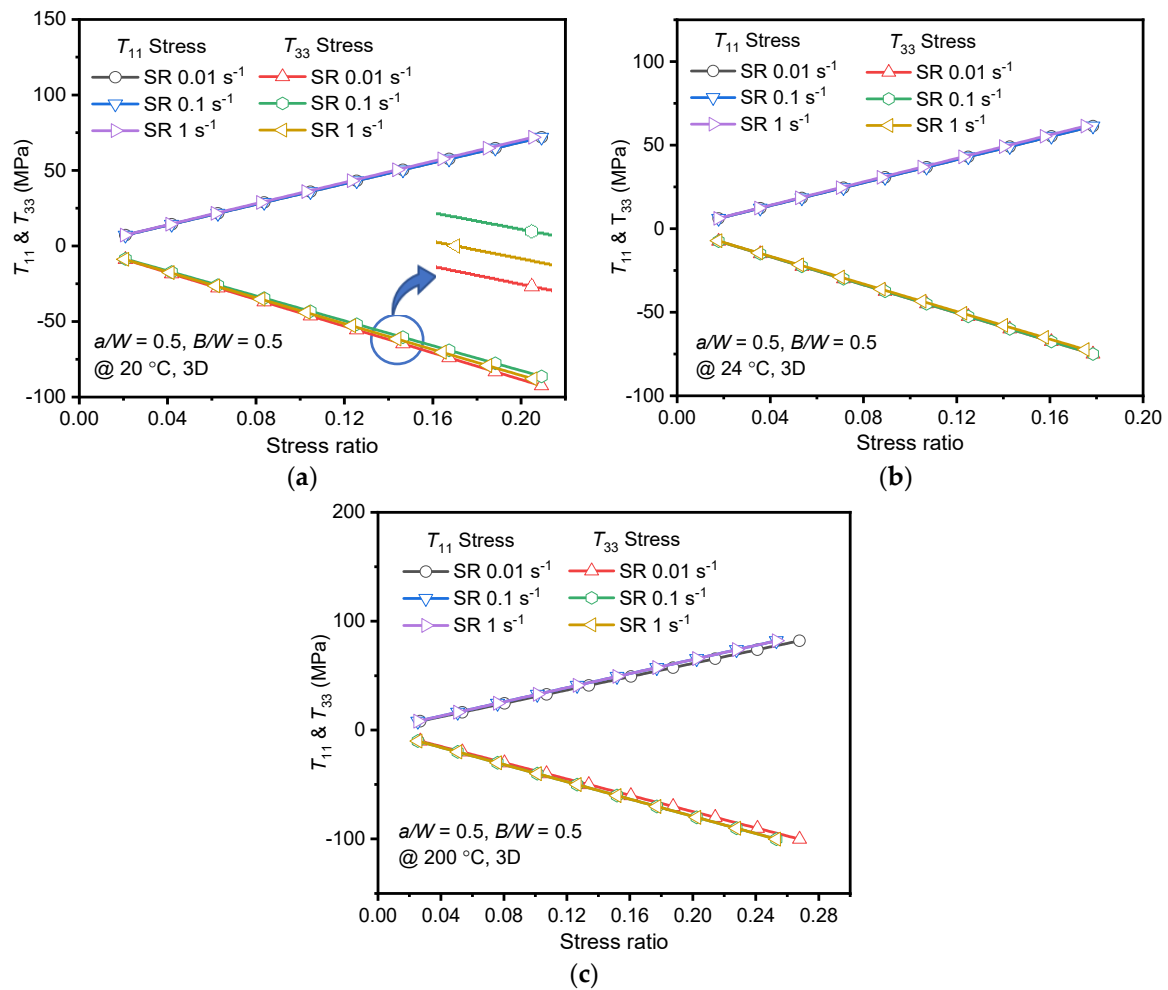
Figure 8. T_{11} and T_{33} at specimen thickness center obtained using FEA for different strain rates vs. Stress ratio (**a**) @ −20 °C; (**b**) 24 °C; (**c**) 200 °C.

At 24 °C and 200 °C, both constraint parameters were unaffected (very marginal difference) by the strain rate variation, as observed in Figure 8b,c. However, T_{33} variations between the strain rates at −20 °C were relatively substantial. At −20 °C, between the strain rates, a difference of 2.4% was found for T_{33}. T_{33} variation depended on Poisson's ratio and Young's modulus (material property) of the alloy at different strain rates. Eventually, the crack driving and constraint parameters were less sensitive to strain rate variations.

Strain rate effect on T_{11} variation is negligible as in-plane constraint depends on specimen type, geometry, and loading type only. Furthermore, the variation of hydrostatic stress along the uncracked ligament is studied at different strain rates. It is observed that no variations are found at different strain rates. The negligible variation of T_{11} can also be attributed to the uniform state of stress at the crack front and minimal variation of yield stress (or stress ratio as depicted in the graph) between the strain rates. However, the T_{33} variation is quite measurable at different strain rates for −20 °C, as shown in Figure 8a, owing to the variations in material property (both Young's modulus and yield stress). Positive T_{11} results in a lower plastic zone at the crack tip and influences the specimen's unstable crack growth. Similarly, negative T_{33} results in loss of constraint at the crack tip.

Since the crack front plasticity is restricted in LEFM regime, the state of stress may be unaltered due to strain rate variations at identical temperatures. The current serrated stress-strain curves may affect the plasticity ahead of the crack front and can be accounted in Elastic-Plastic Fracture Mechanics (EPFM) regime.

3.2.2. Effect of Temperature

The variation of K_I at different temperatures for quasi-static strain rates is plotted in Figure 9. The K_I variation is linearly increased with an increase in stress ratio as expected, and the nature of variation was the same for all temperatures considered. At the peak stress ratio, the difference between K_I at 200 °C and −20 °C is 5.1%, 5.16%, and 7.31% at strain rates 0.01, 0.1, and 1 s^{-1}, respectively. However, the variation of K_I was minimum (around 4%) for the temperatures 24 °C and 200 °C at all strain rates. Notably, the temperature effect was highest at strain rate 1 s^{-1} and in the decreasing order of 1: 0.1: 0.01 s^{-1}. The substantial variation of K_I at sub-zero temperatures indicates that for identical load conditions, the AA2050-T84 alloy is more prone to fracture failure than the other two temperatures as it possesses lower K_{IC}.
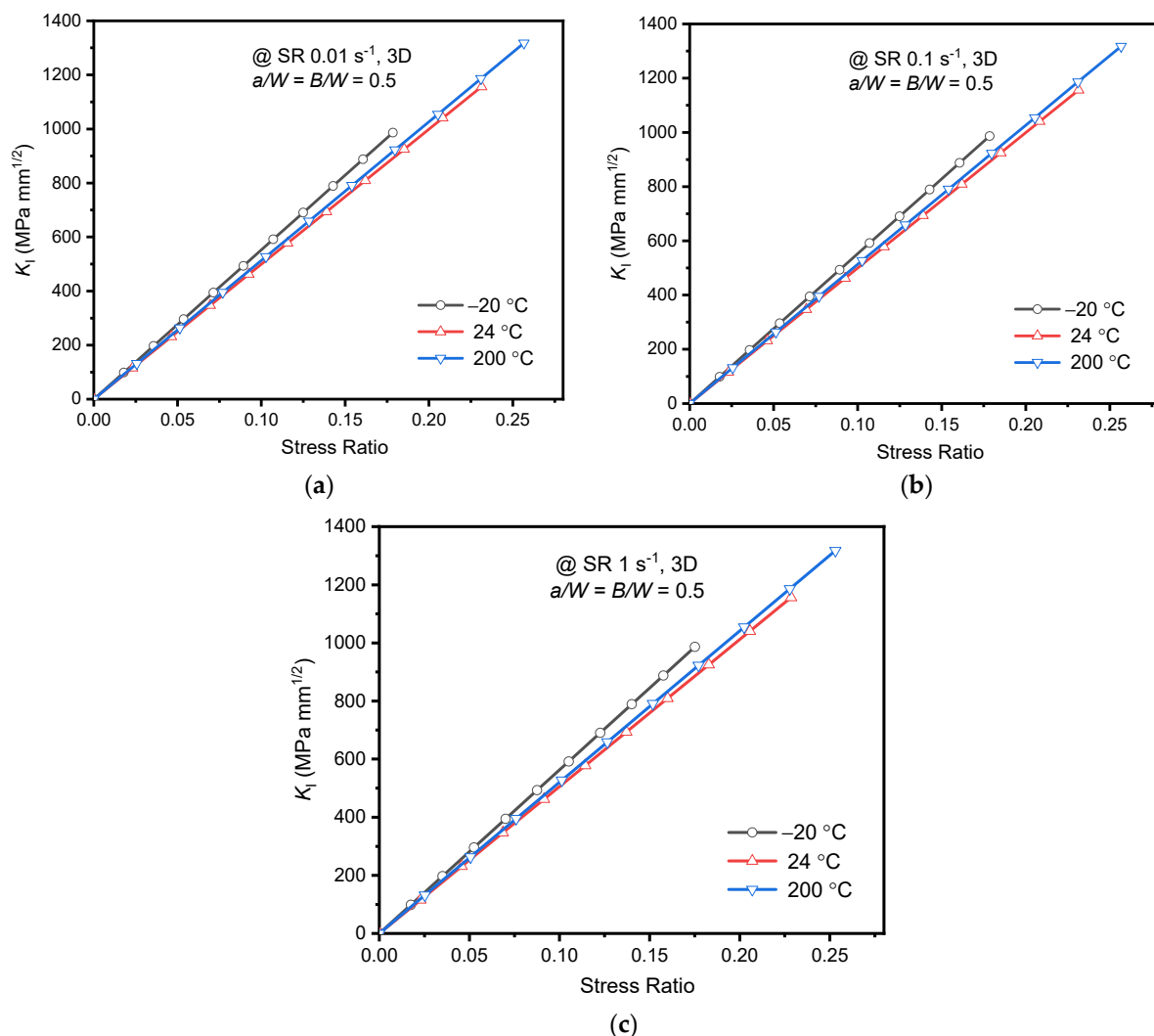

(a)

(b)

(c)

Figure 9. K_I at specimen thickness center obtained using FEA for different temperature vs. Stress ratio (**a**) SR 0.01 s^{-1}; (**b**) SR 0.1 s^{-1}; (**c**) SR 1 s^{-1}.

Similarly, Figure 10 shows the variation of T_{11} and T_{33} at different temperatures for quasi-static strain rates. The variation of T_{11} and T_{33} were almost identical at 24 °C and 200 °C at quasi-static strain rates. At 200 °C, the T_{11} was less subtle and owed lower in-plane constraints than the −20 °C, and 24 °C. Chemin et al. [6] have related dislocations gathered along the grain boundaries, led to stress concentrations under loading and promoted the lower fracture toughness of the AA2050-T84 alloy at sub-zero (−56 °C) temperature. Similarly, in the current analysis, the sensitivity of fracture toughness and in-plane constraint against the stress ratio is highest at −20 °C. The sensitivity may be

associated to crack front stress concentrations at grain boundaries at $-20\,^{\circ}\mathrm{C}$ and can be accounted through constraint parameters as shown in the current numerical analysis. However, the T_{11} and T_{33} variations seem identical for strain rates 0.01 and $1\,\mathrm{s}^{-1}$ through Figure 10a,c at $-20\,^{\circ}\mathrm{C}$. Eventually, T_{11} and T_{33} in combination with K_I is maximum at $1\,\mathrm{s}^{-1}$ compared to $0.01\,\mathrm{s}^{-1}$. Thus, the highest constraint associated with numerically obtained K_I of the AA2050-T84 alloy at $-20\,^{\circ}\mathrm{C}$ is $1\,\mathrm{s}^{-1}$. This behavior also resulted in the lower K_{IC} at $-20\,^{\circ}\mathrm{C}$ than $24\,^{\circ}\mathrm{C}$.
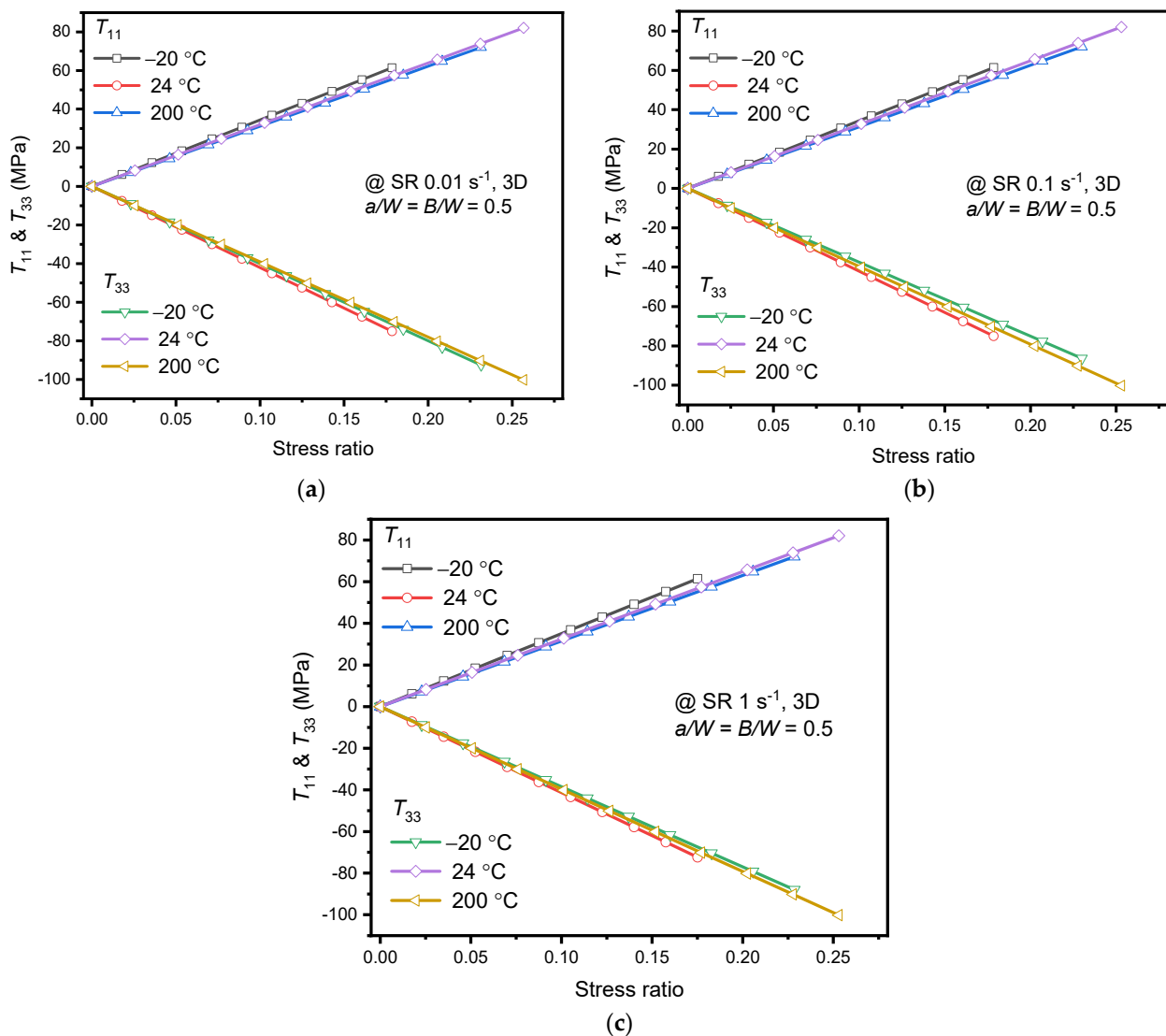

Figure 10. T_{11} and T_{33} at specimen thickness center obtained using FEA for different temperature vs. Stress ratio (**a**) SR $0.01\,\mathrm{s}^{-1}$; (**b**) SR $0.1\,\mathrm{s}^{-1}$; (**c**) SR $1\,\mathrm{s}^{-1}$.

In summary, the major constraint loss was observed for temperature variation compared to quasi-static strain rate variations. Moreover, at $-20\,^{\circ}\mathrm{C}$, AA2050-T84 alloy possesses lower K_{IC} with the highest in-plane crack tip/front constraint compared to the other two temperatures. This behavior of the alloy makes it vulnerable to fracture failure in cryogenic (sub-zero) applications at a strain rate $1\,\mathrm{s}^{-1}$.

4. Conclusions

In the present study, the tensile and fracture behavior of the 50 mm thick (2-inch) AA2050-T84 plate was considered at various temperatures for quasi-static strain rates. Tensile tests revealed the sensitivity of mechanical properties towards the strain rates and

temperatures. Positive strain rate dependency was observed for temperatures considered on yield stress and ultimate tensile stress of the alloy. A maximum of 2% increase in yield stress was noticed between strain rates at −20 °C. The lowest strain rate sensitivity of around 0.5% was witnessed at room temperature. Notably, the ultimate stress variation between the strain rates for temperatures was less than 1%. However, Young's modulus and % elongation were negative strain rate dependent. The maximum decrease of Young's modulus up to 10% was noticed at 200 °C. The minimum Young's modulus variation was witnessed at −20 °C between the strain rates.

Temperature sensitivity towards tensile behavior of the AA2050-T84 alloy was noticed. The maximum yield stress variation of 10–11% was witnessed between room temperature and −20 °C. Notably, the yield stress increase was only up to 3% between room temperature and 200 °C. Similarly, for ultimate stress, the variation was up to 7.5% between room temperature and −20 °C. However, the reduction of Young's modulus up to 18% was noticed between room temperature and 200 °C. This implies that yield and ultimate stress are quite substantial at −20 °C compared to other temperatures, making the AA2050-T84 alloy vulnerable at sub-zero temperatures. Moreover, an increase in strain rate prompts the decrease in % elongation, implying the brittle behavior of the alloy at higher strain rates.

The crack driving and constraint parameters are less sensitive to strain rate variations. However, at −20 °C, crack characterizing and constraint parameters to strain rate variations were moderately considerable. The temperature effect is highest at strain rate 1 s^{-1} and in the decreasing order of $1 : 0.1 : 0.01 \text{ s}^{-1}$.

Overall, the AA2050-T84 alloy tensile and fracture performance obtained through experimental and numerical analyses exhibited the dependency on strain rates and temperatures. Hence, these mechanical properties of the alloy strongly influence the damage tolerance design of spars and wings of the aircraft. The authors believe that the current results concerning strain rates and temperatures will help in understanding the performance-related issues of AA2050-T84 alloy reported in aircraft applications.

References

1. Wanhill, R.J.; Bray, G.H. Aerostructural design and its application to aluminum–lithium alloys. In *Aluminum-Lithium Alloys*, 1st ed.; Prasad, N.E., Gokhale, A., Wanhill, R.J.H., Eds.; Butterworth-Heinemann: Oxford, UK, 2014; pp. 27–58.
2. Lynch, S.P.; Wanhill, R.J.; Byrnes, R.T.; Bray, G.H. Fracture toughness and fracture modes of aerospace aluminum–lithium alloys. In *Aluminum-Lithium Alloys*, 1st ed.; Prasad, N.E., Gokhale, A., Wanhill, R.J.H., Eds.; Butterworth-Heinemann: Oxford, UK, 2014; pp. 415–455.
3. Edgar, A.; Starke, J.R. Historical Development and Present Status of Aluminum Lithium Alloys. In *Aluminum-Lithium Alloys*, 1st ed.; Prasad, N.E., Gokhale, A., Wanhill, R.J.H., Eds.; Butterworth-Heinemann: Oxford, UK, 2014; pp. 3–26.

4. Dorin, T.; Vahid, A.; Lamb, J. Aluminium lithium alloys. In *Fundamentals of Aluminium Metallurgy*, 1st ed.; Lumley, R.M., Ed.; Woodhead Publishing: Duxford, UK, 2018; pp. 387–438.

5. Hafley, R.A.; Domack, M.S.; Hales, S.J.; Shenoy, R.N. *Evaluation of Aluminum Alloy 2050-T84 Microstructure and Mechanical Properties at Ambient and Cryogenic Temperatures*; Technical Report for NASA; Langley Research Center: Hampton, VA, USA, August 2011.

6. Chemin, A.E.; Afonso, C.M.; Pascoal, F.A.; Maciel, C.D.; Ruchert, C.O.; Bose Filho, W.W. Characterization of phases, tensile properties, and fracture toughness in aircraft-grade aluminum alloys. *Mater. Des. Process. Commun.* **2019**, *1*, 1–3. [CrossRef]

7. Mirza, M.S.; Barton, D.C.; Church, P. The effect of stress triaxiality and strain-rate on the fracture characteristics of ductile metals. *J. Mater. Sci.* **1996**, *31*, 453–461. [CrossRef]

8. Clausen, A.H.; Børvik, T.; Hopperstad, O.S.; Benallal, A. Flow and fracture characteristics of aluminium alloy AA5083–H116 as function of strain rate, temperature and triaxiality. *Mater. Sci. Eng. A* **2004**, *364*, 260–272. [CrossRef]

9. Singh, N.; Singh, V. Effect of temperature on tensile properties of near-α alloy Timetal 834. *Mater. Sci. Eng. A* **2008**, *485*, 130–139. [CrossRef]

10. Khan, A.S.; Liu, H. Strain rate and temperature dependent fracture criteria for isotropic and anisotropic metals. *Int. J. Plast.* **2012**, *37*, 1–5. [CrossRef]

11. Anderson, D.; Winkler, S.; Bardelcik, A.; Worswick, M.J. Influence of stress triaxiality and strain rate on the failure behavior of a dual-phase DP780 steel. *Mater. Des.* **2014**, *60*, 198–207. [CrossRef]

12. Roth, C.C.; Mohr, D. Effect of strain rate on ductile fracture initiation in advanced high strength steel sheets: Experiments and modeling. *Int. J. Plast.* **2014**, *56*, 19–44. [CrossRef]

13. Rincon, E.; Lopez, H.F.; Cisneros, M.M.; Mancha, H.; Cisneros, M.A. Effect of temperature on the tensile properties of an as-cast aluminum alloy A319. *Mater. Sci. Eng. A* **2007**, *452*, 682–687. [CrossRef]

14. Natesan, E.; Ahlström, J.; Manchili, S.K.; Eriksson, S.; Persson, C. Effect of Strain Rate on the Deformation Behaviour of A356-T7 Cast Aluminium Alloys at Elevated Temperatures. *Metals* **2020**, *10*, 1239. [CrossRef]

15. Pandya, K.S.; Roth, C.C.; Mohr, D. Strain rate and temperature dependent fracture of aluminum alloy 7075: Experiments and neural network modeling. *Int. J. Plast.* **2020**, *135*, 102788. [CrossRef]

16. Ekabote, N.; Kodancha, K.G.; Kudari, S.K. Suitability of Standard Fracture Test Specimens for Low Constraint Conditions. *Conf. Ser. Mater. Sci. Eng.* **2021**, *1123*, 012033. [CrossRef]

17. Ekabote, N.; Kodancha, K.G.; Revankar, P.P. Elastic-plastic fracture analysis of anisotropy effect on AA2050-T84 alloy at different temperatures: A numerical study. *Frat. Integrita Strutt.* **2022**, *16*, 78–88.

18. Gupta, M.; Alderliesten, R.C.; Benedictus, R. A review of T-stress and its effects in fracture mechanics. *Eng. Fract. Mech.* **2015**, *134*, 218–241. [CrossRef]

19. O'dowd, N.P.; Shih, C.F. Family of crack-tip fields characterized by a triaxiality parameter—I. Structure of fields. *J. Mech. Phys. Solids.* **1991**, *39*, 989–1015. [CrossRef]

20. Hutař, P.; Seitl, S.; García, T.E.; Fernández-Canteli, A. Experimental and numerical analysis of in-and out-of plane constraint effects on fracture parameters: Aluminium alloy 2024. *Appl. Comput. Mech.* **2013**, *7*, 53–64.

21. Fernández-Canteli, A.; Giner, E.; Fernández-Zúniga, D.; Fernández-Sáez, J. A unified analysis of the in-plane and out-of-plane constraints in 3-D linear elastic fracture mechanics. In Proceedings of the 19th European Conference on Fracture, Kazan, Russia, 26–31 August 2012.

22. Kudari, S.K.; Kodancha, K.G. 3D Stress intensity factor and T-stresses (T11 and T33) formulations for a Compact Tension specimen. *Frat. Integrita Strutt.* **2017**, *11*, 216–225. [CrossRef]

23. Wang, X. Elastic T-stress for cracks in test specimens subjected to non-uniform stress distributions. *Eng. Fract. Mech.* **2002**, *69*, 1339–1352. [CrossRef]

24. Neimitz, A.; Galkiewicz, J. Fracture toughness of structural components: Influence of constraint. *Int. J. Press. Vessel. Pip.* **2006**, *83*, 42–54. [CrossRef]

25. Galkiewicz, J.; Janus-Galkiewicz, U. The Numerical Analysis of the In-Plane Constraint Influence on the Behavior of the Crack Subjected to Cyclic Loading. *Materials* **2021**, *14*, 1764. [CrossRef] [PubMed]

26. Kim, Y.K.; Oh, B.T.; Kim, J.H. Effects of Crack Tip Constraint on the Fracture Toughness Assessment of 9% Ni Steel for Cryogenic Application in Liquefied Natural Gas Storage Tanks. *Materials* **2020**, *13*, 5250. [CrossRef]

27. *ASTM E399-20*; Standard Test Method for Linear-Elastic Plane-Strain Fracture Toughness of Metallic Materials. ASTM International: West Conshohocken, PA, USA, 2020.

28. Brian Falzon. The Airbus A380 Wing Cracks: An Engineer's Perspective. Available online: https://theconversation.com/the-airbus-a380-wing-cracks-an-engineers-perspective-5318 (accessed on 22 January 2022).

29. Rioja, R.J.; Liu, J. The evolution of Al-Li base products for aerospace and space applications. *Metall. Mater. Trans. A* **2012**, *43*, 3325–3337. [CrossRef]

30. *ASTM E8/E8M-21*; Standard Test Methods for Tension Testing of Metallic Materials. ASTM International: West Conshohocken, PA, USA, 2021.

31. Mouritz, A.P. *Introduction to Aerospace Materials*; Woodhead Publishing Limited: Cambridge, UK, 2012; pp. 454–468.

32. Ekabote, N.; Kodancha, K.G. Temperature and test specimen thickness (TST) effect on tensile and fracture behavior of AA2050-T84 alloy. *Mater. Today Proc.* 2021, *in press*. [CrossRef]

33. Dassault Systemes. Abaqus Analysis User Guide. Available online: http://wufengyun.com/v6.14/books/usb/default.htm?startat=pt05ch22s02abm03.html (accessed on 22 January 2022).
34. Farraro, R.; McLellan, R.B. Temperature dependence of the Young's modulus and shear modulus of pure nickel, platinum, and molybdenum. *Metall. Trans. A* **1977**, *8*, 1563–1565. [CrossRef]
35. Borges, M.F.; Antunes, F.V.; Prates, P.A.; Branco, R.; Vojtek, T. Effect of Young's modulus on fatigue crack growth. *Int. J. Fatigue* **2020**, *132*, 105375. [CrossRef]
36. Abd El-Aty, A.; Xu, Y.; Guo, X.; Zhang, S.H.; Ma, Y.; Chen, D. Strengthening mechanisms, deformation behavior, and anisotropic mechanical properties of Al-Li alloys: A review. *J. Adv. Res.* **2018**, *10*, 49–67. [CrossRef] [PubMed]
37. Kavale, S.M.; Kodancha, K.G.; Ekabote, N. Effect of Poisson's ratio on KI, T11 and T33 for SENB and CT specimen–A FE study. *Procedia Struct. Integr.* **2019**, *14*, 584–596. [CrossRef]